



Measurement of picometer-scale mirror dynamics

BABAK SAIF,¹ DAVID CHANEY,² PERRY GREENFIELD,^{3,*} MARCEL BLUTH,⁴ KYLE VAN GORKOM,³ KOBY SMITH,² JOSH BLUTH,⁴ LEE FEINBERG,¹ JAMES C. WYANT,^{5,6} MICHAEL NORTH-MORRIS,⁶ AND RITVA KESKI-KUHA¹

¹NASA/GSFC, 8800 Greenbelt Road, Greenbelt, Maryland 20771, USA

²Ball Aerospace, 1600 Commerce Street, Boulder, Colorado 80301, USA

³Space Telescope Science Institute, 3700 San Martin Drive, Baltimore, Maryland 21218, USA

⁴SGT, 7515 Mission Drive, Suite 300, Seabrook, Maryland 20706, USA

⁵College of Optical Sciences, University of Arizona, Tucson, Arizona 85721, USA

⁶4D Technology, 3280 East Hemisphere Loop, Suite 146, Tucson, Arizona 85706, USA

*Corresponding author: perry@stsci.edu

Received 15 May 2017; revised 7 July 2017; accepted 10 July 2017; posted 12 July 2017 (Doc. ID 294954); published 3 August 2017

A high-speed interferometer has been designed and built to measure the dynamics of the James Webb Space Telescope primary mirror system currently under testing. This interferometer is capable of tracking large absolute motion (i.e., piston) of the mirror's entire surface over orders of magnitudes of wavelengths displacement. Preliminary tests have shown it to be capable of measuring dynamic effects on the level of tens of picometers reliably. This paper reports the details of test setup to do so, the data system used to collect and process the data, and the algorithms to distill the dynamics motions detected. The results that were obtained are presented and followed by a discussion of the conclusions and potential applications of this measurement technique. © 2017 Optical Society of America

OCIS codes: (120.3180) Interferometry; (120.3940) Metrology; (120.4630) Optical inspection; (120.5050) Phase measurement; (120.6650) Surface measurements, figure; (120.7280) Vibration analysis.

<https://doi.org/10.1364/AO.56.006457>

1. INTRODUCTION

One possible successor to the James Webb Space Telescope (JWST) is an observatory that combines general ultraviolet-optical infrared (UVOIR) astrophysics with the search for life on habitable earth-like exoplanets using a large-aperture segmented telescope. Work on this problem began in 2009 as a potential advanced telescope large-aperture space telescope (ATLAST) architecture [1]. Early work focused on a scalable 9.2 m segmented telescope that could launch in a Delta IV heavy launch vehicle and the work has recently progressed to a 12 m segmented telescope. The most significant architectural driver beyond the aperture size is the 10^{-10} contrast required to block out the bright stars sufficiently to detect dim Earth-like planets. Achieving this requires a combination of a high-throughput coronagraph with sufficient bandpass and wavelength range to perform spectroscopic surveys and a very stable telescope that maintains the <10 pm stability required for most observations. Achieving picometer stability, thermal and dynamic, is done through passive and active means in a system of multilevel hierarchies.

An important first step in achieving this level of stability is the ability to achieve picometer-level metrology that can characterize the thermal and dynamic behavior of the optical system being designed and built, starting from the smallest components to subsystems, and finally, the system as a whole.

This requires a metrology system capable of measuring thermal and dynamical changes of both diffuse and reflective surfaces of the elements of the system to picometer accuracy. It is unjustifiable to assume that the stability of a system scales linearly with levels of stimulus over orders of magnitude. More precisely, the transfer function of a system is not constant over orders of magnitude in the level of the stimulus. This paper shows the picometer dynamical characterization of a spare segment of the JWST primary mirror array. This mirror is a 1.5 m gold-coated hexagonal beryllium mirror with a radius of curvature of approximately 16 m. The level of precision is achieved using a new custom-made high-speed interferometer (HSI). This interferometer has been designed and built by 4D Technology [2] in collaboration with the Goddard Space Flight Center.

This paper focuses on the issue of measuring dynamics at high precision. We outline the experimental setup, data collection, handling, and processing that were employed to study the benefit of using the HSI to make such measurements in the following sections. We conclude with a discussion about the results obtained and their meaning.

2. OPTOMECHANICAL SETUP

A. Basic Setup

The optomechanical test arrangement used for the mirror is that of a classical interferometric center-of-curvature test. This

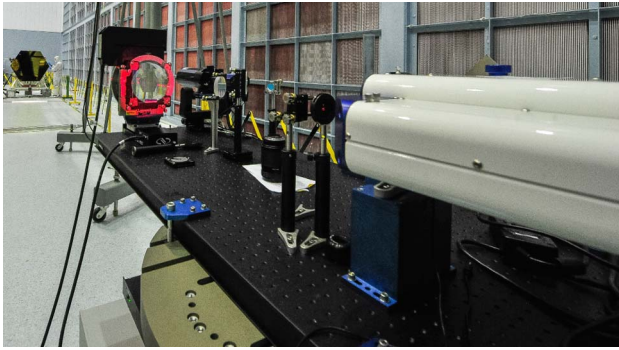


Fig. 1. This photograph shows all the optical elements in the test setup including the HSI, CGH (framed in red), and test mirror (hexagonal mirror on the far left).

involves placing an interferometer with a diverging lens such that its focus is coincident with the center of curvature of the mirror under test. If the test mirror were a sphere, then all optical test rays would be normal to the mirror surface. However, the tested mirror is an off-axis asphere. Therefore, a diffractive null optic is required to convert the interferometer's spherical test beam to an aspheric one. For this test, a computer-generated hologram (CGH) was used as the null optic. When the mirror is placed at the correct location relative to the CGH and interferometer, then all optical test rays are normal to the mirror surface and retrace their path through the test layout. (A detailed description of the use of CGHs for mirror testing may be found in Ref. [3].) In this instance, the CGH is placed 0.890 m from the mirror segment focus. Deviations in the mirror figure create optical path differences that show up as phase differences in the interferometer, both spatially and temporally. Figure 1 shows a photograph of the test setup including the HSI, CGH, and the JWST mirror segment.

The HSI obtains simultaneous measurements of the interference at four separate phases. Therefore, the HSI can obtain relative spatial phase differences in one exposure. These differences are then converted to a surface figure map. Figure 2 shows a schematic diagram of the HSI.

B. Alignment Procedure

Distinguishing figure error from alignment error is critical and is accomplished by precisely aligning the mirror under test to the CGH in six degrees of freedom. This alignment is broken

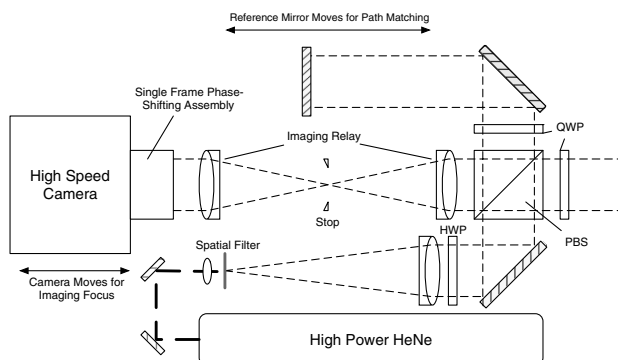


Fig. 2. Schematic diagram of the HSI optical system.

up into three steps. The tip/tilt of the mirror is aligned using interferometer tilt fringes as feedback. The decenter and clocking of the mirror relative to the CGH is achieved using an alignment camera system. A more detailed description of the alignment procedure may be found in Ref. [2].

C. Stimulus Setup and Data Collection

The mirror is stimulated at the back of the mirror using a stinger that is attached to a suspended shaker (see Fig. 3). A triaxial arrangement of accelerometers is attached to the side of the mirror and independently measure the acceleration and displacement of the edge of the mirror due to stimuli. The test control system and data flow are represented in Fig. 4. Data are collected from the following systems:

- HSI (an image stream);
- A Dataphysics unit that collects:
 - force measurements from the stinger;
 - values from all accelerometers.

It is important that all these data be properly synchronized. This is achieved by triggering the stimulus, the collected force and accelerometer data, and the image exposures on the HSI from the same triggering signal. A function generator sends a string of pulses that serves to trigger the data acquisition system (DAQ) and the HSI. The pulses in the signal also control the HSI frame rate (each image must be individually triggered). The DAQ is triggered only on the first pulse. Once triggered, the DAQ sends an excitation signal to the stinger to provide the



Fig. 3. This photograph shows how the stinger was positioned and connected to the mirror support structure (the back side of the mirror is visible on the extreme right and has a triangular rib structure). The stinger is the cylindrical object mounted in the red bracket on the extreme left. There is a force sensor interposed between the stinger rod and the structure.

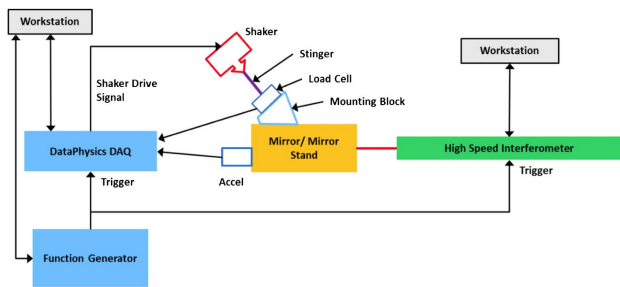


Fig. 4. This schematic diagram shows the relationship of the components of the test setup.

programmed excitation to the system under test as well as starting the collecting of data. Comparisons of the timing of the recorded stimulus and observed HSI mirror displacements show them to be coincident within approximately $10\ \mu\text{s}$.

Determining the dynamics requires obtaining the difference in the surfaces from the two consecutive exposures in an absolute sense—in other words, the absolute spatial difference between the surface measurements at two times. This has typically been difficult for interferometers, since the surface changes at a faster rate relative to wavelength than the interferometer is capable of repeating observations. The high sample rate of the HSI permits this interferometer to keep pace with the dynamics of the surface and maintain differences between exposures comfortably within a wavelength.

In principle, a static surface figure that does not deform will only show rigid body dynamics when observed with the HSI. However, this assumes that the alignment between the interferometer system and the mirror remains the same over the consecutive measurements. Since the mirror is under stimuli and physically moves, misalignment errors are not necessarily negligible for the desired uncertainties on the order of picometers. The leakage of the static figure alignment errors into dynamic effects is tracked by using the information on dynamics (both from the interferometer and accelerometer) to determine if there is any significant secondary effect on the dynamic measurement. Another potential source of error (particularly over longer times) is environmental disturbances. These may be background vibrations, or changes in temperature, airflow, and other factors that may affect the measurements.

3. DATA HANDLING

The interferometer is capable of generating a great deal of data in a short time. The maximum frame rate depends on the image size permitted. The data presented in this paper generally used a frame size of 719×719 that allowed a maximum reliable frame rate of 900 Hz. Data typically were collected for 10 s for each measurement. As a result, each measurement results in approximately 4.2 GB of data collected. The limit on how long a measurement can run is determined by the amount of memory in the data acquisition computer, 20 GB in this instance. The results presented here are averaged over 10 such measurements.

Data volumes in this range require substantial computing and storage facilities. The data were transferred to computing server after the completion of a measurement, then processed on up to 256 cores.

The raw data format is a 4D-Technology special-purpose format that is read on the computer servers and converted into other special-purpose formats, generally one file per frame. Most of the processing software was written in Python with heavy use of numpy, matplotlib, scipy and astropy [4–7], and has been written to use all available processing cores to reduce the total time needed to process a measurement data set.

4. ALGORITHM

A. Basic Phase Computation

Since the interferometer obtains all four delay phases simultaneously through use of a spatial carrier method before the camera, it is possible to compute the phase from a single exposure by decomposing the image into the four separate phase planes, interpolating between the samples and applying the standard expressions to compute the phase from these planes. The result is a wrapped phase image, and spatial phase unwrapping must be used to recover continuous surface profiles. Figure 5 shows the results of the different steps in that process. Figure 6 shows the spectrum measured by the force sensor for a fixed frequency stimulus at 87.3 Hz.

B. Ellipse to Circle Correction

Small errors in the phase-shifting element can result in high-frequency print-through on the reconstructed mirror surface (see Fig. 7). To minimize phase extraction error, we follow the treatment in Refs. [8,9]. We generate Lissajous figures from the pairs of orthogonal interference signals in the raw frame, fit an ellipse to find the decenter and eccentricity, and recenter and stretch the signals to a circle (see Fig. 8) before computing the

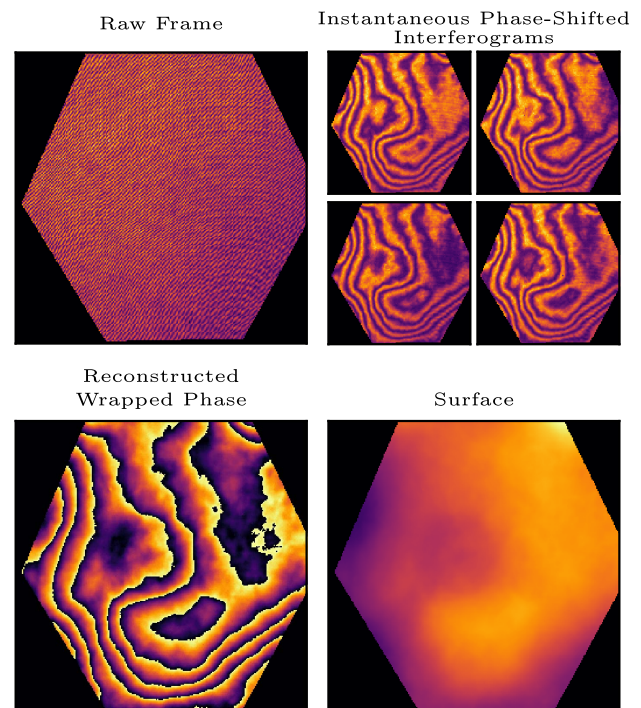


Fig. 5. Single HSI frame comprises four interlaced phase-shifted interferograms that are converted (with an ellipse-to-circle correction to account for phase error) into a wrapped phase image that can be unwrapped to a surface profile.

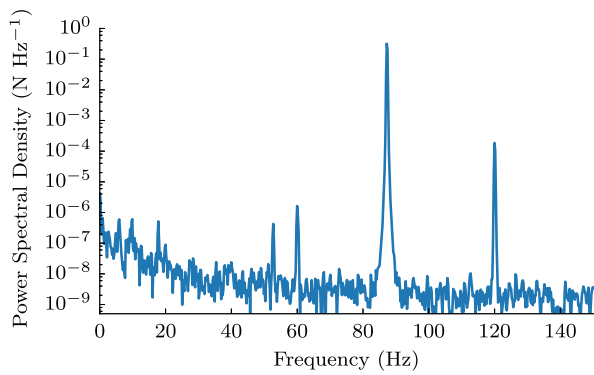


Fig. 6. Spectrum of the input stimulus, a sine dwell at 87.3 Hz.

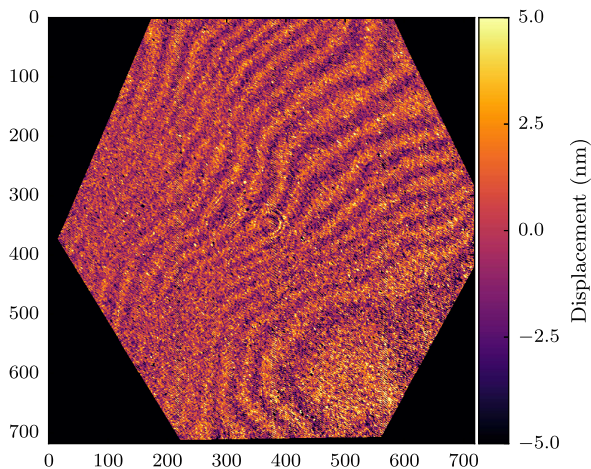


Fig. 7. Difference image of the reconstructed mirror surface with and without the ellipse-to-circle correction, showing high-frequency print-through at the 2.3 nm RMS level, most of which is subsequently removed by the E2C correction.

wrapped phase. To account for the possibility that the error varies across the detector spatially as well as temporally, we compute a unique correction for each pixel on a rolling temporal basis.

C. Temporal-Spatial Unwrapping

After the ellipse-to-circle correction and computation of the wrapped phase, each data set can be understood as a cube of phases $p(x, y, t)$ defined over two spatial dimensions and one temporal. Each pixel is unwrapped independently along the temporal axis, with the relative offset of each pixel determined by a spatial unwrap of the first frame. If the maximum allowable velocity

$$v_{\max} = \frac{\lambda}{4} f_{\text{sampling}} \quad (1)$$

is exceeded, temporal unwrapping fails and discontinuities appear on the mirror surface (see Fig. 9). If, however, some portion of the mirror never exceeds v_{\max} , every surface can be completely recovered. By inspection of the final frame, the displacement at a region (x_b, y_b) of the mirror that shows no discontinuities is adopted as a temporal baseline. A more

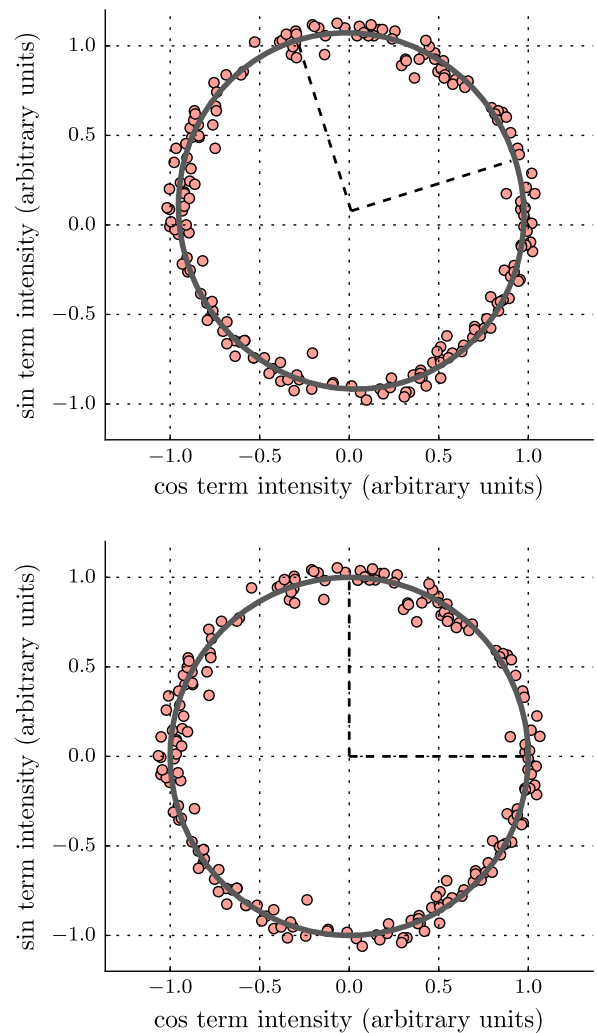


Fig. 8. Top, example of an ellipse fit to the sine and cosine interference signals showing a slightly ellipticity and decenter; bottom, data after the E2C correction.

stringent method is to examine the histogram of observed phase differences in time; regions with no velocity violations will have a sufficiently narrow histogram of values. Typically, both methods are used to ensure that the selected region is satisfactory for temporal unwrapping. In other words, this region is presumed to define the absolute motion of that region correctly in time. Once determined, every frame is spatially unwrapped, and resulting phase of all pixels is offset by a constant value to match the phase value obtained for the baseline region. In this way, absolute displacements are obtained for the whole mirror even if parts of the mirror at times violate the velocity restrictions for doing temporal phase unwrapping. Figure 10 shows a case of a pixel correctly temporally unwrapped (top plot) and one that wasn't but where a residual phase error has been corrected by spatial phase unwrapping.

D. Data Processing

Each data set results in a cube with two spatial dimensions and one temporal dimension. We take the fast Fourier transform (FFT) of the temporal displacement at each pixel to create a

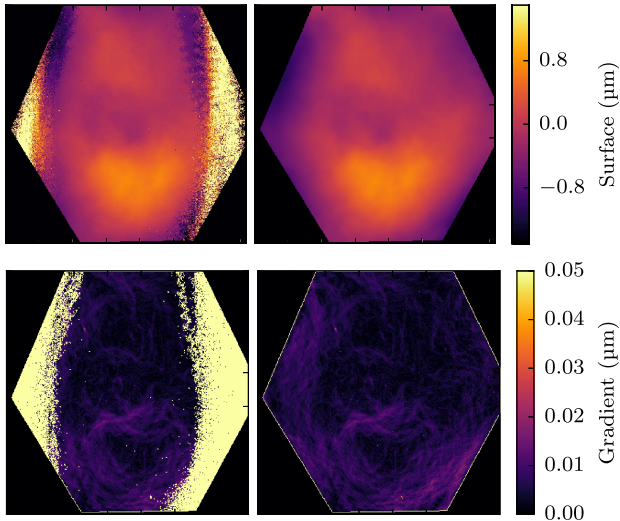


Fig. 9. Top, mirror surface at the final frame of a 10-s data set, showing (left) a region where temporal unwrapping failed and (right) the region after spatial unwrapping; bottom, corresponding surface gradient images used to diagnose the surface region where velocity violations have occurred.

cube of surfaces spanning the frequencies of the FFT. Since for each data set the stinger has a different phase, we cannot simply average the data sets together without correcting for this variation. This is done by dividing each frequency cube, represented as complex values, by the FFT of the measured force signal for all spatial pixels, normalized to 1 (without normalization, it would represent the transfer function). This division places all data sets on a common phase basis so that the results can be averaged.

The frequency of interest (i.e., the stinger frequency) is selected by zeroing all other frequencies in the cube, and the result is transformed back to the temporal domain. Zernike

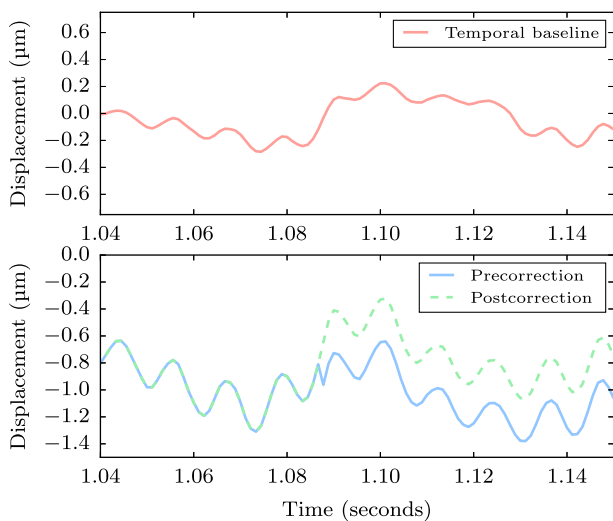


Fig. 10. Top, measured displacement of a single pixel against time on a part of the mirror surface that never experiences a velocity violation; bottom, displacement of a single pixel that experiences a velocity violation, before and after the spatial unwrapping correction and temporal baselining to the “good” pixel above.

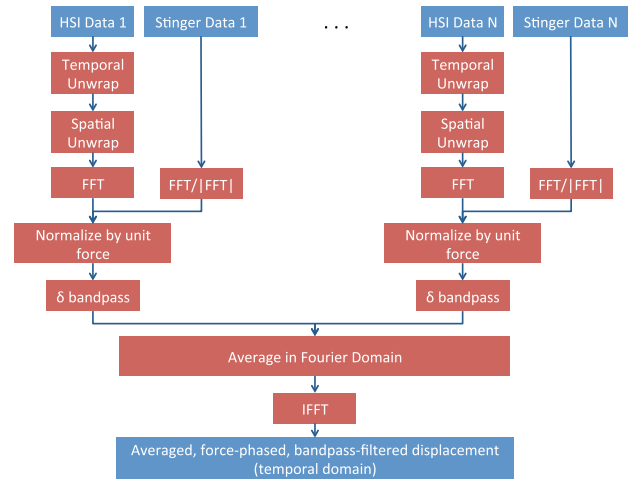


Fig. 11. Processing flow for combining multiple HSI data sets. After unwrapping, each data set is individually FFTed, phase-shifted by the stimulus phase, and frequency selected to isolate the forcing frequency. These data sets are then averaged in the Fourier domain and inverted to the temporal domain, where Zernike polynomials are fit to each frame.

polynomials are then fit to each surface. Each Zernike term is then fit to obtain the amplitude and phase relative to the stinger. The same processing (excluding the step that phases each data set to the input force) is repeated for background measurements. (Note that one can equivalently fit Zernikes first in the temporal domain, perform an FFT on each Zernike time series, and divide by the normalized force signal to obtain the amplitude and phase for each term determined at the stinger frequency.)

Figure 11 outlines the steps of this processing schematically.

Shown in Fig. 12 is the residual image obtained after subtracting the first 30 Zernike terms as seen at one instant in time. From this image, one can see three general kinds of spatially correlated structures. There are small defects, either in the detector or in the optical system that result in very localized deviations, or diffraction-like circular structures, particularly

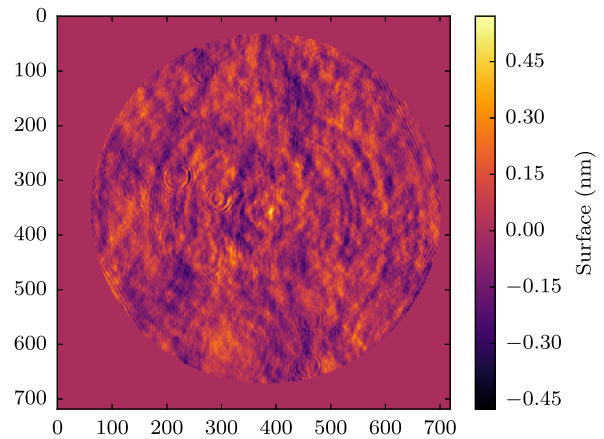


Fig. 12. Residuals of the measured mirror surface at 87.3 Hz at one particular time, with the fit Zernike surfaces cumulatively removed up to and including the Z30 term. It is apparent that coherent spatial structures remain.

just left of center. These have a very high spatial frequency. The second kind are roughly circular grooves or hills. These have a fairly high spatial frequency in the radial direction. The last kind are roughly consistent with Zernike functional shapes not yet subtracted and have comparatively low spatial frequency. Recall that these are all dynamic terms, i.e., structures that have frequency corresponding to the stimulus frequency.

5. RESULTS AND DISCUSSION

At what level of accuracy is it possible to measure dynamic components? The principal approach is to compare the amplitude of measured Zernike terms when the structure was mechanically stimulated to what was measured when no stimulus was present. To get the spatial RMS contribution of each Zernike term to the time-varying surface variance, we first average each Zernike component over each of the 10 measurement runs as a complex number that encapsulates both its amplitude and phase relative to the normalized forcing signal. The amplitude of the resulting complex value is then divided by the canonical factor to convert it to the equivalent spatial RMS. When squared, these terms represent the contribution to the total surface variance after averaging in time. Since different Zernike terms have different phases, their contributions to the surface variance vary over a cycle of the stimulus, but since these are orthogonal functions, the time-averaged total surface variance is simply a sum of the individual Zernike surface variances; hereafter, it is assumed that all spatial RMS values are simply related to the total time-averaged RMS, although we have not applied the typical $\sqrt{2}$ factor to the values plotted; thus the plotted values are not time-averaged values.

The relative contributions of each term can be illustrated by showing how the residual RMS varies with the Zernike term by successively removing Zernike components from the net dynamic figure as a function of the Zernike term and computing the resulting RMS. More specifically, we obtain the RMS that remains from subtracting the first N Zernike terms by subtracting from the total variance the sum of the variance of the first N Zernike terms, and then plotting that as a function of N . That is:

$$\text{Residual RMS}(N) = \sqrt{\text{Total RMS}^2 - \sum_{i=1}^N Z_{\text{rms}_i}^2}. \quad (2)$$

Figures 13 and 14 show this residual RMS as a function of a Zernike term. The cumulative plots for the background case show that after Z3, the remaining RMS is below 30 pm, dropping slowly to below 20 pm at Z30 and above.

Figures 15 and 16 show the power spectral density (PSD) traces of the first 12 Zernike terms for the 87.3 Hz stimulus and background cases to illustrate the response over the whole spectrum rather than at one frequency. Figures 17 and 18 show the stimulated and background values on the same log plot for 87.3 Hz and 65 Hz.

Do these measured Zernike terms for the stimulated case reflect real dynamic content or are these just artifacts of noise or other errors? Since the background-only measurements show very low values, any other explanation must be somehow coupled to the existence of the stimulus. One possible coupling

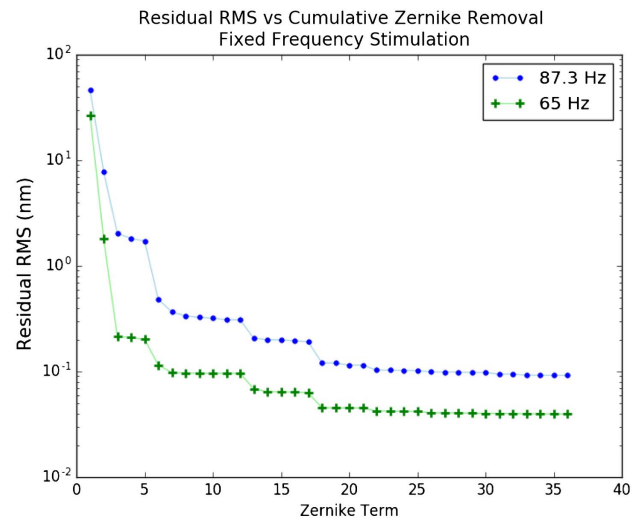


Fig. 13. Plotted is the residual spatial RMS present after subtracting the first N dynamic Zernike terms from the observed data with the stimulus present. In this case the residuals are time averaged.

is rigid body motions of the mirror, resulting in apparent dynamic Z terms at higher orders (i.e., Z1, Z2, and Z3 terms, as well as lateral motions not measured directly by the interferometer). The consequential rigid body displacements could result in measurable distortions due to misalignments with the optical measuring system, and the CGH in particular.

A. Modeling Dynamic Misalignment

The optical model of the measurement setup permits us to compute the effect of any dynamic misalignments. The optical model is based on one constructed to support testing JWST primary mirror segment assembly (PMSA) segments in ambient and cryogenic conditions at the Marshall Space Flight Center XRCF facility.

The Code V model is a linear model of the optical system that includes the CGH element and the measured surface of the

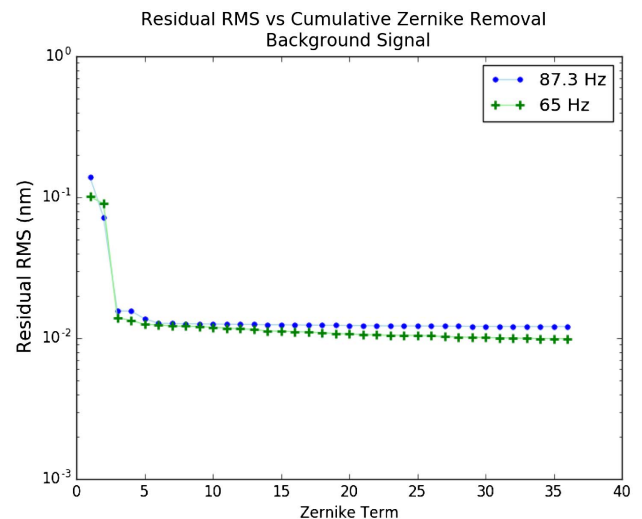


Fig. 14. Equivalent spatial RMS residuals for the case where no stimulus is present (other than environmental vibrations). In this case the residuals are time averaged.

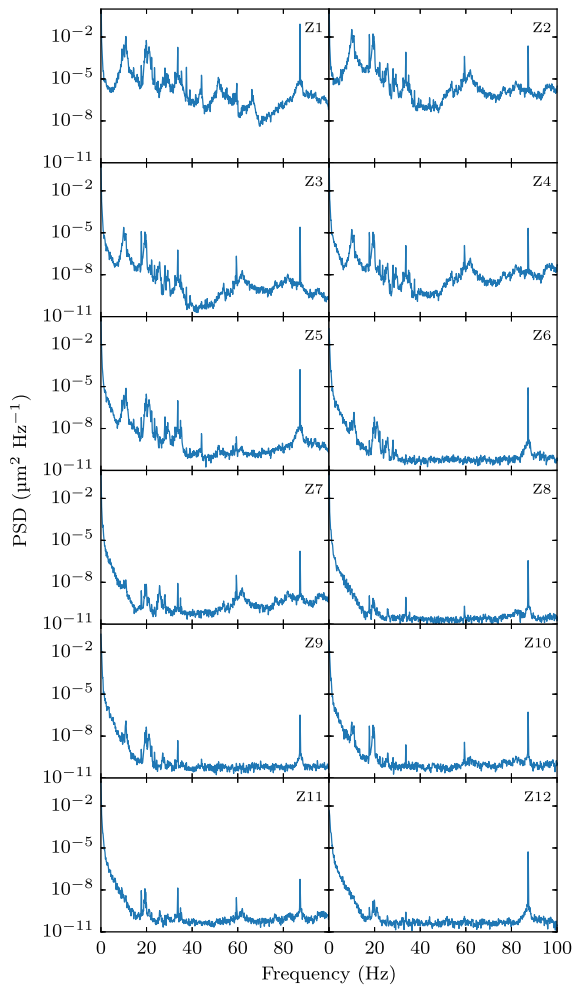


Fig. 15. Spectrum of Zernike coefficients 1 through 12, showing a sharp response at the 87.3 Hz stimulus frequency. Zernike polynomials were fit to all frames in each individual data set, and each PSD above represents the averaged PSD computed from the individual data sets.

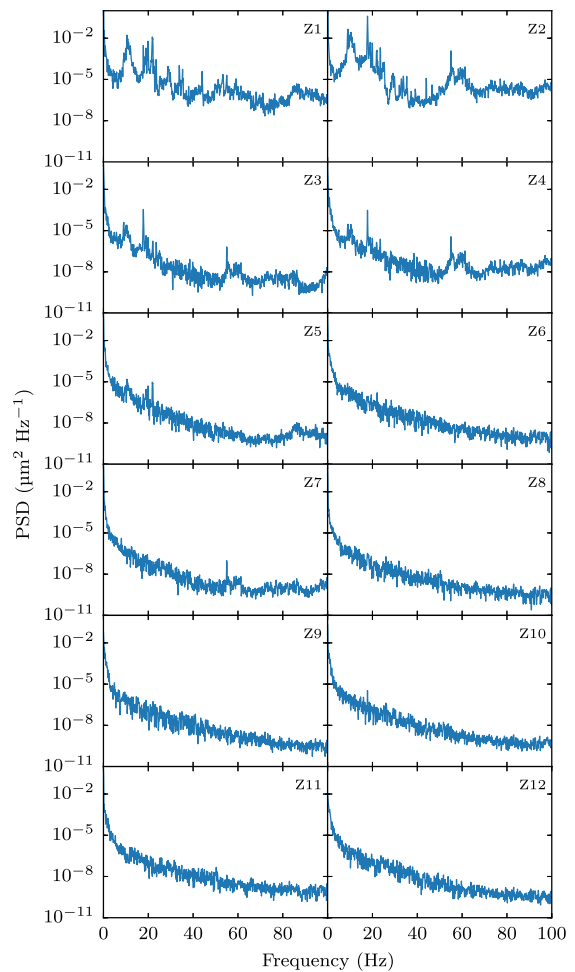


Fig. 16. Spectrum of Zernike coefficients 1 through 12, for HSI data sets with no input stimulus. Compare to Fig. 15 (in particular, the response at 87.3 Hz). Zernike polynomials were fit to all frames in each individual data set, and each PSD above is the averaged PSD computed from the individual data sets.

mirror at ambient temperatures. The perturbations are introduced to the model one at a time, and the induced change in the resulting Zernike representation is computed (in effect, fitting Zernikes to the difference between the wavefront error with the perturbation and the wavefront error without).

The effects due to mirror motions were estimated by taking the maximum displacement observed from the interferometer data and the integration of the accelerometer data in all three dimensions for translation, and in all three rotation axes (two tilt, and one clocking), and apply these to the optical model to see the resultant changes in the observed mirror figure for the extreme offset. Code V was used to compute the resulting changes in the observed mirror figure, and the first 36 Zernike terms fit to the inscribed circle of the observed hex shape.

The obtained Zernike coefficients predicted were first assumed to be at their largest 95% confidence levels (the modeling introduces some uncertainty) and then added for all six rigid body motions (absolute values). Since it is unlikely that these contributions are perfectly coherent, this overestimates

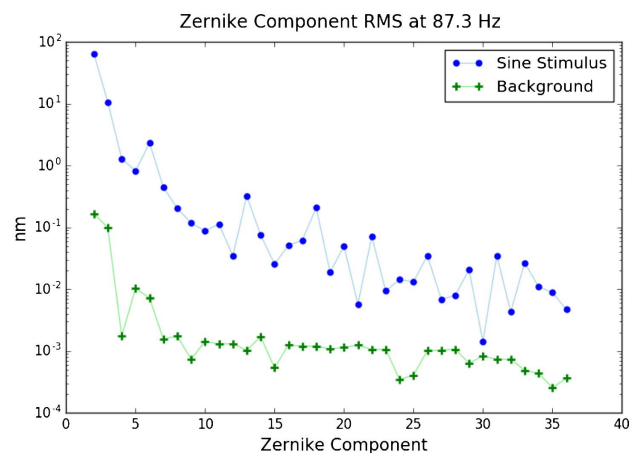


Fig. 17. Plotted are the dynamic Zernike term RMS values for two different cases: (1) the case where a fixed frequency sinusoidal stimulus is present, and (2) the case where no such stimulus is present.

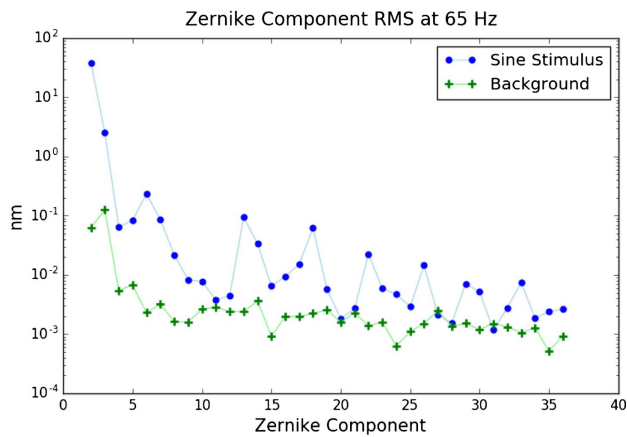


Fig. 18. Same information as plotted in Fig. 17, except for the 65 Hz observations.

the effect. The results are shown in Figs. 19 and 20 for the 87.3 Hz and 65 Hz data (as spatial RMS values).

B. Modeling Structural Dynamics

A structural analysis was completed with the objective of estimating the mirror surface dynamic response. The analysis process emulated to a practical extent the test data reduction and evaluation. The analysis employed the JWST validated the PMSA structural dynamics model that was the accepted system element at the time of this writing.

The validated JWST PMSA finite element structural model was used to assess the response of the mirror resulting from the testing stimulus. The structural model contained three-node triangular elements for the mirror and bar elements for the flexures. The base of the flexures was constrained to a rigid body boundary condition (i.e., a NASTRAN RBE2). Translations of 1 mm in each of the three global axis directions and rotations of 1 mrad about each of the three global axis directions were applied independently at both 65 Hz and 87.3 Hz. For each of these cases, the complex surface displacement in the optical direction of the test was extracted.

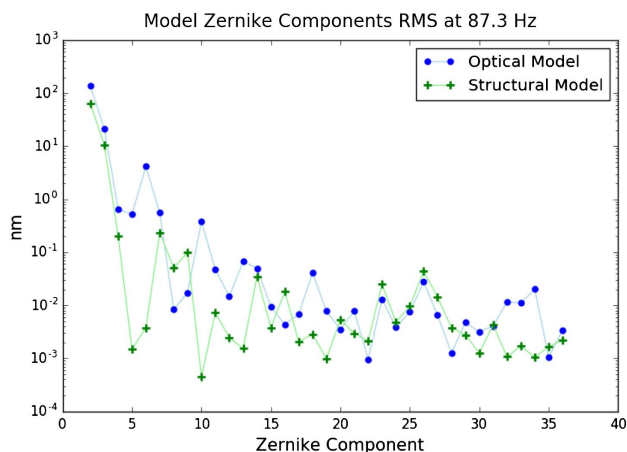


Fig. 19. Plotted are the ratios of the measured Z terms to motion-induced Z terms at 87.3 Hz.

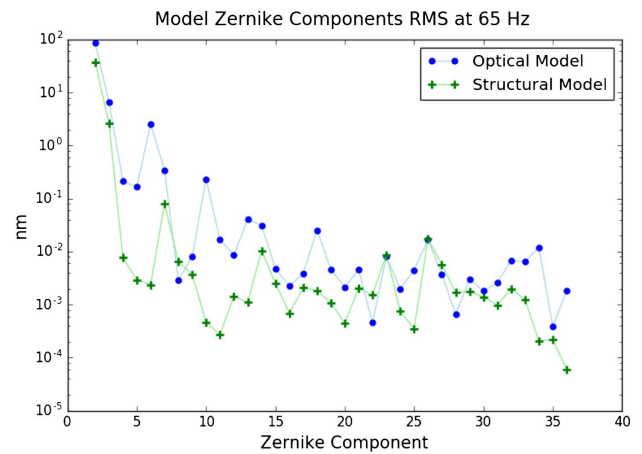


Fig. 20. Corresponding values for 65 Hz as shown in Fig. 19.

These resulting surface displacements for each of the spatial translations and rotations were scaled by the ratio of the corresponding displacement values used for the optical model. The scaled displacements were then summed using the relative phases measured from the test of the six degrees of freedom throughout the frequency period (which was not done for the optical dynamics estimate).

The spatial RMS for the first 36 Zernike terms was extracted from each of the 87.3 Hz and 65 Hz predicted surface displacements. The results show exact agreement with the two tilts term measured in the test, because these values are boundary conditions to the dynamics model. The agreement at these points confirms the target input to model was accomplished correctly.

C. Comparison of Models and Data

The structural analysis results were combined with the optical analysis results previously discussed to provide an estimate of the predicted size of the measured Zernike terms. This combination was accomplished by direct summation of the amplitudes of the two models at each Zernike. The comparison of the combined results to the test data is presented in Figs. 21 and 22.

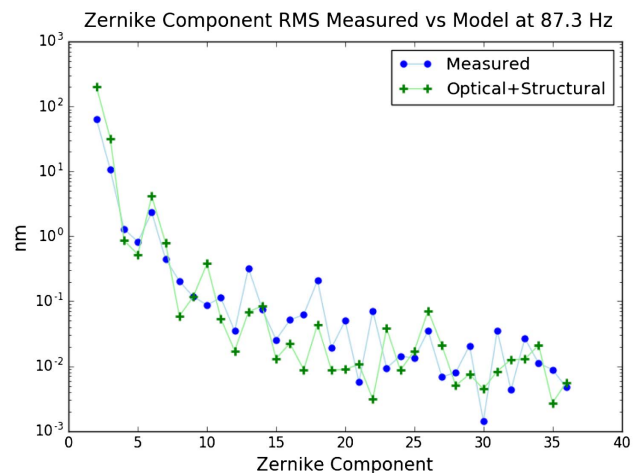


Fig. 21. Plotted is the comparison between the measured Zernike RMS terms and the sum of the corresponding optical and structural dynamic model terms.

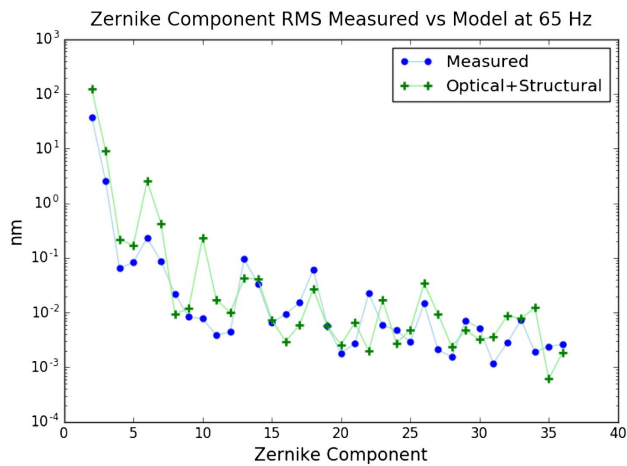


Fig. 22. Corresponding values for 65 Hz as shown in Fig. 21.

The comparison of the combined predictive model to the test shows remarkable agreement both in trend of the drop in Zernike term magnitude and the magnitudes. Also note that good agreement is achieved on order of tens of picometers in many cases. We caution that this is not a rigorous prediction of the size of the effect, but the close agreement does suggest that these two effects may account for all that is seen in the measurements.

It is also clear that understanding real effects at picometer levels requires careful simulation of the secondary effects of rigid body motion with regard to the optical model. If one can measure that sufficiently well, then it can be subtracted from the observed values and much higher precision may be obtained. Future experiments will enable high precision measurements of rigid body motion using multiple accelerometers.

To summarize the conclusions obtained:

- It is possible to use the HSI to measure dynamic terms to the order of tens of picometers.
- Many of the measured Zernike terms are not explained by background noise or rigid-body motion-induced effects.

- Two possible explanations are dynamic mirror deformations or nonlinear behavior in the system.

Funding. Goddard Space Flight Center (GSFC).

Acknowledgment. We gratefully acknowledge the James Webb Space Telescope and the Ultra-stable Structures projects and specifically Mario Perez at NASA Headquarters for the funding support for this effort.

REFERENCES

1. N. Rioux, H. A. Thronson, L. Feinberg, H. P. Stahl, D. C. Redding, A. L. Jones, J. A. Sturm, C. M. Collins, A. Liu, and M. Bolcar, "Future large-aperture UVOIR space observatory: reference designs," *J. Astron. Telesc. Instrum. Syst.* **2**, 041214 (2016).
2. B. Saif, D. Chaney, W. Smith, P. Greenfield, W. Hack, J. Bluth, A. Van Otten, M. Bluth, J. Sanders, R. Keski-Kuha, L. Feinberg, M. North-Morris, and J. Millerd, "Nanometer level characterization of the James Webb Space Telescope optomechanical systems using high-speed interferometry," *Appl. Opt.* **54**, 4285–4298 (2015).
3. J. H. Burge, "Advanced techniques for measuring primary mirrors for astronomical telescopes," Ph.D. dissertation (University of Arizona, 1993).
4. S. van der Walt, S. C. Colbert, and G. Varoquaux, "The NumPy array: a structure for efficient numerical computation," *Comput. Sci. Eng.* **13**, 22–30 (2011).
5. T. E. Oliphant, "Python for scientific computing," *Comput. Sci. Eng.* **9**, 10–20 (2007).
6. J. D. Hunter, "Matplotlib: a 2D graphics environment," *Comput. Sci. Eng.* **9**, 90–95 (2007).
7. T. P. Robitaille, E. J. Tollerud, P. Greenfield, M. Droettboom, E. Bray, T. Aldcroft, M. Davis, A. Ginsburg, A. M. Price-Whelan, W. E. Kerzendorf, A. Conley, N. Crighton, K. Barbary, D. Muna, H. Ferguson, F. Grollier, M. M. Parikh, P. H. Nair, H. M. Günther, C. Deil, J. Woillez, S. Conseil, R. Kramer, J. E. H. Turner, L. Singer, R. Fox, B. A. Weaver, V. Zabalza, Z. I. Edwards, K. A. Bostroem, D. J. Burke, A. R. Casey, S. M. Crawford, N. Dencheva, J. Ely, T. Jenness, K. Labrie, P. L. Lim, F. Pierfederici, A. Pontzen, A. Ptak, B. Refsdal, M. Servillat, and O. Streicher, "Astropy: a community python package for astronomy," *Astron. Astrophys.* **558**, A33 (2013).
8. C. T. Farrell and M. A. Player, "Phase step measurements and variable step algorithms in phase-shifting interferometry," *Meas. Sci. Technol.* **3**, 953–958 (1992).
9. V. I. Guzhov, S. P. Il'yinykh, D. S. Khaidukov, and A. R. Vagizov, "Eliminating phase-shift errors in interferometry," *Optoelectr. Instrum. Data Process.* **47**, 96–101 (2011).